Solid ^{7}Li-NMR and *in situ* XRD studies of the insertion reaction of lithium with tin oxide and tin-based amorphous composite oxide

Solid ^{7}Li-NMR and *in situ* XRD studies of the insertion reaction of lithium with tin oxide and tin-based amorphous composite oxide

Kazuhiko Furuya[1,3]**, Keizou Ogawa**[1]**, Yasushi Mineo**[1]**, Akihiro Matsufuji**[1]**, Jun Okuda**[1] **and Tomoki Erata**[2]

[1] Ashigara Research Laboratories, Fuji Photo Film Co. Ltd, 210 Nakanuma, Minami Ashigara, Kanagawa 250-0193, Japan
[2] Division of Molecular Chemistry, Graduate School of Engineering, Hokkaido University, Kita13, Nishi8, Kita-ku, Sapporo, Hokkaido 060-0813, Japan

E-mail: huruya@ashiken.fujifilm.co.jp (K Furuya)

Abstract
The lithium insertion reactions with tin (II) oxide (SnO) and tin-based composite oxide (abbreviated as TBCO) are studied by solid ^{7}Li-NMR Knight shift, T_1 and $T_{1\rho}$ relaxation rate, TEM and *in situ* XRD methods. By the insertion reaction for SnO, the lithium oxide and β-tin are produced first at Li/Sn = 2; at Li/Sn = 3 to 6 the products are not simple and a mixture of $LiSn_2$, LiSn, Li_5Sn_2 and Li_7Sn_2 alloys is detected during the insertion. For the TBCO, which is revealed as amorphous, mainly constituted by randomly distributed very short-range (order of 10^{-9} m) regions by TEM observation, it is found that electrochemically inserted lithium forms Li_2O and produces metallic tin (Sn) in the first step (Li/Sn < 2), then the highly ionic lithium–tin alloys, Li_7Sn_2 (and Li_7Si_2), are produced in the second step (Li/Sn > 2). During the second step, the Li/Sn ratio of formed lithium–tin alloy is kept at almost 4. By the analyses of ^{7}Li NMR Knight shifts, line shape and *in situ* XRD, the lithium-inserted TBCOs are characterized as almost amorphous and mixtures of highly ionic components.

1. Introduction

Rechargeable lithium ion batteries are useful for cellular phones, lap top computers, electric vehicles and many other products and their market size is growing rapidly on a worldwide scale. Idota *et al* have reported the high capacity lithium batteries, which employs a new type of anode material, a tin-based amorphous composite oxide (referred to as TBCO in the following text), and have discussed the fundamental characteristics of TBCO [1, 2]. Although

[3] Corresponding author.

the TBCOs show high capacity as compared with the traditional graphite compounds in the battery system, the details of the lithium insertion reaction mechanism remain uncertain.

Dahn *et al* have studied the lithium insertion reactions into the tin oxide compounds using the *in situ* XRD method and reported that reduction of Sn (II) to metallic tin (0) and formation of lithium oxide (Li_2O) occur first by introducing lithium [3, 4]. They have also concluded that the various lithium–tin alloys with Li/Sn ratios up to 4.4 (Li_2Sn_5, LiSn, Li_7Sn_3, Li_7Sn_2 and $Li_{22}Sn_5$) have been formed during the lithium insertion reaction and the Li/Sn ratio is correlated to the inserted lithium quantity. The *in situ* XRD gives plenty of information on the crystalline tin (II) oxide compounds. However, this method is not applicable to amorphous materials such as TBCO. For SnO and SnO containing glass, *in situ* [119]Sn Mössbauer measurements are reported by Dahn *et al* to study the reaction of lithium [5].

The NMR method is widely used for studying the electronic structure or ionic motion for both crystalline and amorphous materials from the microscopic point of view. The ^{7}Li-NMR Knight shift and the electric resistivity of various lithium–tin alloys at molten state have been reported [6, 7]. According to van der Marel *et al* , the ^{7}Li-NMR Knight shift drastically drops from 265 ppm (lithium metal) to 60 ppm (Li_4Sn alloy), and then rises to about 110 ppm (higher lithium–tin ratio alloys). On the other hand, the electric resistivity shows the reverse behaviour and reaches its maximum at Li_4Sn alloy. Through analysis of the Knight shift and the electric resistivity of liquid lithium–tin alloys, van der Marel *et al* have concluded that the electron transfer reaction from lithium to tin occurs in Li_4Sn alloy. Because of the loss of the usual metallic alloy character, they have called this Li_4Sn alloy 'ionic alloy' or 'zero alloy'. The charge transfer from lithium to tin in the ionic alloy has been confirmed by the neutron diffraction measurement [8]. These phenomena have been observed between alkali metal (I) and the group IV binary alloy systems and a review has been published by van der Lugt [9], but these reports are not commonly known in other fields of research.

In this report, in order to understand the mechanism of lithium insertion reactions and to improve the electrochemical properties of TBCO as an anode material, characterization of the state of lithium ion in the tin oxide and TBCO compounds has been performed using solid ^{7}Li-NMR, transmission electron microscopy (abbreviated as TEM) and *in situ* XRD methods.

2. Experiment

Several lithium–tin alloys were supplied from Honjyo Kinzoku Industry Corporation. The Li/Sn ratios of these alloys were confirmed by x-ray diffraction and ICP analysis as 0.5 ($LiSn_2$), 1.0 (LiSn), 2.5 (Li_5Sn_2), 3.5 (Li_7Sn_2) and 4.4 ($Li_{22}Sn_5$), respectively [10–13]. The tin (II) oxide (SnO) sample was purchased from Tokyo Chemical Industry Corporation and was used without further purification. Each of these alloys or SnO was mixed with graphite (KS6), acetylene black as the electric conductor and polyvinylidene fluoride (PVDF) with the weight ratio of 83:9:3:5. The slurry material was dried at 373 K for 30 minutes and then ground into powder. A tablet of this material having 1.33×10^{-4} m^2 surface area was prepared and mounted in the *in situ* cell. The polypropylene sheet was used as a separator, and ethylene carbonate (EC) and diethyl carbonate (DEC) were used as a nonaqueous electrolyte solution. The TBCO samples were analysed in the form of a coin type battery or *in situ* XRD cell, and the composition was represented as $Sn_{0.8}Si_{0.5}B_{0.3}P_{0.2}Al_{0.2}O_x$.

The crystal structures were analysed by using a RINT2500 diffractometer (Rigaku) with a Cu Kα x-ray tube. The *in situ* XRD cell was charged to 0.0 V by a constant current mode of 31.9 A kg^{-1} or 9.3 A kg^{-1} for tin (II) oxide. The charging currents of the lithium ion were 42.4 A kg^{-1} and 12.3 A kg^{-1} for TBCO. The charging and discharging cycles were repeated using the HJ-201B charge/discharge unit (Hokuto Denko Corporation).

A 4000-EX transmission electron microscope (JEOL) was used to observe TBCO particles. The powder sample deposited on the grid was observed at the magnification of 150 000 and the photographic film image was enlarged fivefold to get the first intermediate image. This film was then processed to make the second intermediate image by contact exposure to increase the contrast of the image. It was enlarged fivefold again to get the final image and the total magnification was 3 750 000.

^{7}Li-NMR measurements were mainly carried out by a Bruker MSL300 NMR spectrometer equipped with a variable temperature unit, operating at 116.6 MHz for [7]Li nuclei. The NMR spectra were obtained by using the conventional solid echo sequence (90_x–90_y) with 2.3–2.5×10^{-6} s pulse length. The spin–lattice relaxation time T_1 was measured by the inversion recovery method combined with the solid echo method (180_x–90_x–90_y pulses). For examining the frequency dependence of T_1, the rotating frame T_1 relaxation time ($T_{1\rho}$) was measured at 83 kHz rotating frame magnetic field and also a CXP40 NMR spectrometer (Bruker) was used to measure T_1 at 15.5 MHz. The ^{7}Li-NMR spectral data were transferred to an IBM compatible PC and then processed by the Microsoft Excel program. The curve fitting calculation (deconvolution) was included in this process employing both the Lorentzian curve and the Gaussian curve.

3. Results and discussion

3.1. Lithium–tin alloys

The ^{7}Li-NMR shift of the solid lithium–tin alloys measured at room temperature is shown in figure 1. In the solid lithium–tin alloys, the ^{7}Li-NMR shift (the Knight shift) greatly depends on the Li/Sn ratio and the minimum value of 7 ppm is found in Li_7Sn_2 alloy. This value is much smaller than that of the molten state (∼60 ppm, [6]) and almost the same as that of the fully ionic lithium chloride (∼1 ppm) in the aqueous solution, which indicates that the lithium in Li_7Sn_2 alloy has highly ionic character. Since the temperature dependences of the Knight shift of solid lithium–tin alloys were not observed between 300 K and 400 K, the electronic structure of these Li–Sn alloys is fixed in this temperature range. The different behaviour of the Knight shift in Li_7Sn_2 alloy between molten state and solid state can be explained by the large temperature dependence of the Knight shift in the molten state reported in [6].

The temperature dependence of the spin–lattice relaxation time T_1 in the usual metallic alloys can be explained by the well known Korringa relation for degenerate electrons (equation (1), [14]) as

$$K^2 T_1 T = h\gamma_e^2/(8\pi^2 k_B \gamma_n^2) \tag{1}$$

where K is the Knight shift, T is the absolute temperature, h is the Planck constant and γ_e and γ_n denote the electronic and nuclear gyromagnetic ratios, respectively. It is reported that the molten lithium–lead alloys at Li/Pb = 4 show distinct deviation from equation (1) at liquidus temperature (1000 K) [6]. Dupree *et al* [15] derived the Korringa relation for non-degenerate electrons as

$$K^2 T_1 T = h\gamma_e^2/(8\pi^2 k_B \gamma_n^2)\exp[-(E_g - E_f)/k_B T] \tag{2}$$

where E_g and E_f are the energy gap and the Fermi energy, respectively. Figure 2 shows plots of $K^2 T_1 T$ versus $1/T$ for solid lithium–tin alloys. In figure 2, one can draw horizontal lines both for $LiSn_2$ and $LiSn$ alloys above room temperature and for $Li_{22}Sn_5$ alloy below ambient temperature. It is clear that the Korringa relation for degenerate electrons (equation (1)) holds
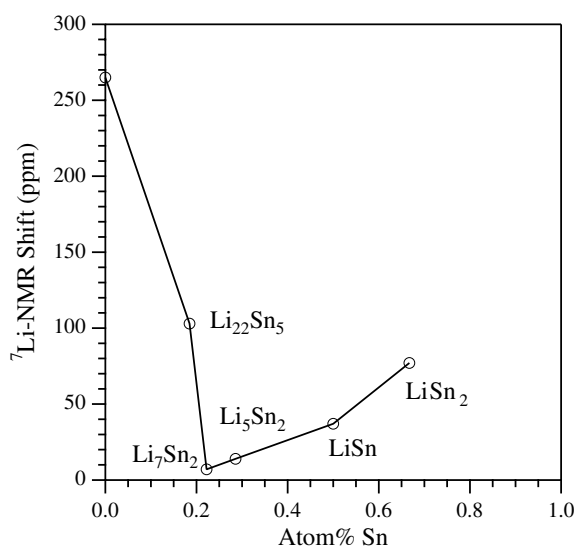
Figure 1. ^{7}Li-NMR Knight shift of solid Li–Sn alloys at room temperature.

for these alloys which show a relatively large Knight shift. The plots of $K^2 T_1 T$ versus $1/T$ do not show the negative slope lines, so the Korringa relation for non-degenerate electrons (equation (2)) does not hold for these alloys.

To consider the relaxation mechanism for solid lithium tin alloys, the dipole–dipole interaction due to the ionic motion is examined. In the dipole–dipole relaxation mechanism for nuclear spin = 1/2, the relaxation rate by the rotational motion is expressed by the following equation [16]:

$$T_1^{-1} = A\tau[1/(1 + \omega^2\tau^2) + 4/(1 + 4\omega^2\tau^2)] \tag{3}$$

where A is a constant and τ and ω are the correlation time and the Zeeman frequency, respectively. If the ionic motion is the Arrhenius type, the correlation time is expressed as

$$\tau = \tau_c \exp(E_a/RT) \tag{4}$$

where E_a is the activation energy and R denotes the gas constant. In the case of $\omega\tau \ll 1$ (the high temperature region), equation (3) is approximated as

$$\ln(T_1^{-1}) = E_a/RT + A'. \tag{5}$$

Similarly, in the case of $\omega\tau \gg 1$ (the low temperature region), equation (3) is expressed as

$$\ln(T_1^{-1}) = -E_a/RT + A''. \tag{6}$$

From equations (5) and (6), E_a is determined by either side of the slope of the plot of $\ln(T_1^{-1})$ versus $1/T$. The relaxation rate shows its maximum at $\omega\tau$ equal to 0.6158, and the inverse of attempt frequency (τ_c) is determined by the T_1 minimum point.

Figure 3 shows the temperature dependence of the T_1 relaxation rate for solid lithium–tin alloys. In figure 3, straight lines can be plotted for Li_7Sn_2 and Li_5Sn_2 alloys which show a small Knight shift. This means the dipole–dipole relaxation mechanism is the main contribution in these alloys instead of Korringa's theory. In this case, these alloys can be called ionic alloys as van der Lugt claims in his review paper [9]. The activation energies of Li_7Sn_2
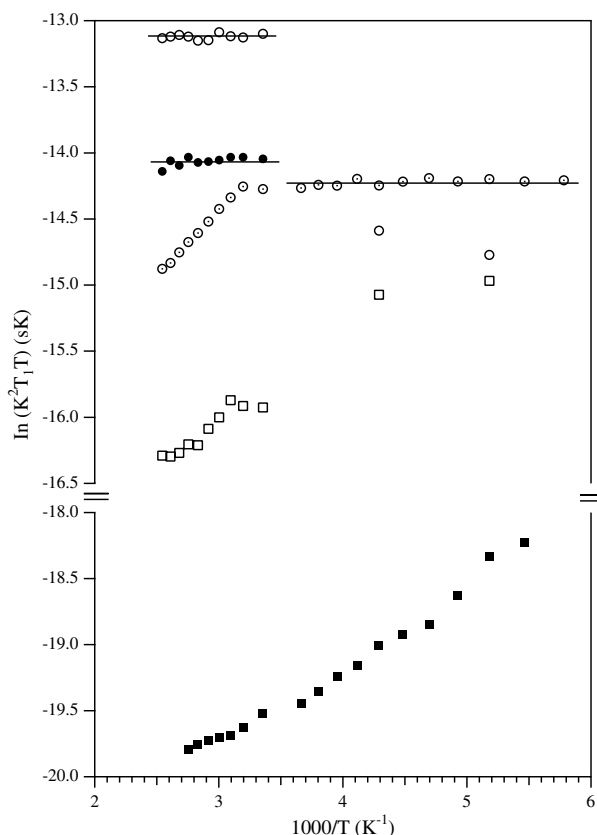
Figure 2. Semilogarithmic plot of $K^2 T_1 T$ versus $1/T$ for solid Li–Sn alloys: $LiSn_2$ ($\bigcirc$), $LiSn$ ($\bullet$), Li_5Sn_2 ($\square$), Li_7Sn_2 ($\blacksquare$) and $Li_{22}Sn_5$ ($\odot$).

and Li_5Sn_2 alloys are determined to be 6.46 and 8.20 kJ mol^{-1}, respectively. For $Li_{22}Sn_5$ alloy, a straight line can be drawn above room temperature. So the dominant relaxation mechanism is estimated to switch from the Korringa relation in the higher temperature region to the dipole–dipole mechanism in the lower temperature region. The activation energy of $Li_{22}Sn_5$ alloy is estimated to be 11.9 kJ mol^{-1}. From van der Lugt's paper [9] and this work, ^{7}Li-NMR Knight shift and T_1 relaxation analysis is found to be a powerful tool for the characterization of the lithium state in Li–Sn alloy systems both for the molten state and the solid state.

3.2. Lithium-inserted tin (II) oxide compounds

The *in situ* XRD patterns of lithium-inserted tin (II) oxide are shown in figure 4. The numbers on the left side indicate the lithium–tin ratios. During the initial step of charging (Li/Sn $\leqslant 2$), the residual tin (II) oxide is observed, the corresponding peaks are shown in figure 4 as + marks and the formation of β-tin is clearly observed ($*$ marks). When two-equivalent lithium is inserted into tin (II) oxide, the x-ray peaks of tin (II) oxide vanish and the peak intensities of β-tin reach the maximum, which is due to the formation of lithium oxides expressed as
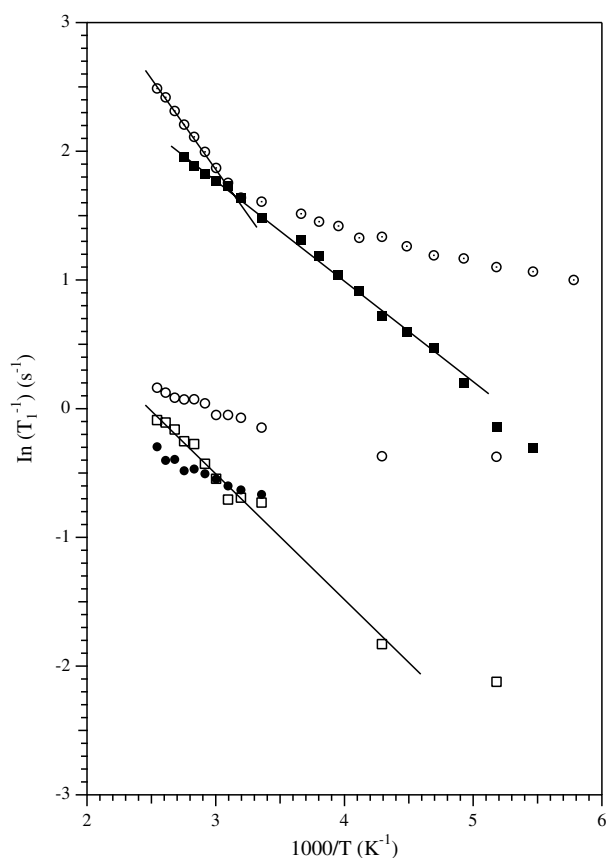
$$SnO + 2Li^+ + 2e^- \rightarrow Sn(\beta) + Li_2O. \tag{7}$$

Figure 3. Temperature dependence of T_1 relaxation rate for solid Li–Sn alloys: LiSn$_2$ (○), LiSn (●), Li$_5$Sn$_2$ (□), Li$_7$Sn$_2$ (■) and Li$_{22}$Sn$_5$ (⊙).

During the second step of charging ($2 < $ Li/Sn $ < 3$), the intensities of the β-tin peak become almost undetectable, and instead of that, the peaks assigned to LiSn alloy are observed at Li/Sn $= 3$ (| marks). The lithium insertion reaction in this region is described as

$$\mathrm{Sn}(\beta) + \mathrm{Li}^+ + \mathrm{e}^- \rightarrow \mathrm{LiSn}. \tag{8}$$

When the Li/Sn ratio is more than 4 (the third step of charging), the XRD patterns show no clear peaks except for those derived from the cell holder, which makes it very difficult to analyse the reaction products. The *in situ* XRD patterns show little change when the current density of the charging process is decreased from 42.4 A kg^{-1} to 12.3 A kg^{-1}. These results indicate that the electric current density does not affect the structure and the reactions of the lithium insertion.

The solid ^{7}Li-NMR spectra of lithium-inserted tin oxide compounds are summarized in figure 5 and figure 6. Figure 6 shows the results of curve fitting of each spectrum. At low lithium–tin ratio (Li/Sn $= 2$), the broad Lorentzian component (abbreviated as L$_b$) and the very broad Gaussian component (alias G$_b$) are observed both at about 0 ppm. From the comparison of the ^{7}Li-NMR shift with that of the authentic sample (Li$_2$O) and the XRD patterns (β-Sn), these two components (L$_b$ and G$_b$) are originated from Li$_2$O formed by the reaction given by equation (7). It is, therefore, estimated that Li$_2$O in β-Sn matrix may have two different
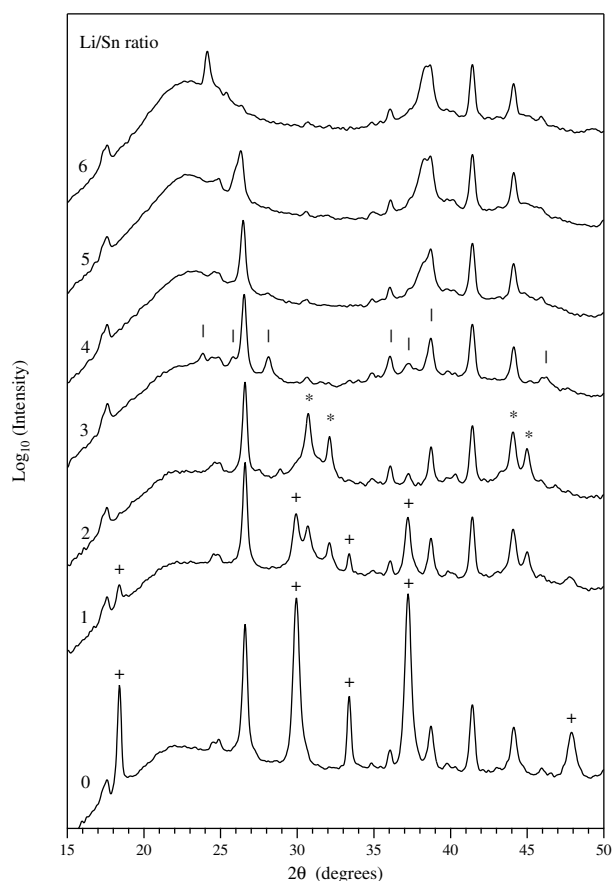
Figure 4. XRD patterns of lithium-inserted SnO. The current density of the charging process is set to 31.9 A kg^{-1}. The peaks marked as + are assigned to tin (II) oxide, those marked as ∗ are for β-tin and those marked as | are for LiSn alloy, respectively.

states, namely, the relatively mobile state (L_b) and the strongly bound state (G_b). Although the spectrum is not shown in this paper, the fact that metallic tin is detected directly at 6700 ppm in the solid ^{119}Sn-NMR spectrum confirms the insertion reaction expressed by equation (8).

When three-equivalent lithium is inserted into tin (II) oxide, the spectrum changes: two new Lorentzian components (alias L_m and L_i) appear at about 60 ppm and at about 0 ppm. The Lorentzian component L_m may be assigned to the mixtures of the metallic LiSn alloy (37 ppm in figure 1) and the metallic LiSn$_2$ alloy (77 ppm in figure 1). Considering the ^{7}Li-NMR shift of Lorentzian component L_i, this component is assigned to be the ionic Li$_7$Sn$_2$ alloy. The residual metallic tin is still observed at 6700 ppm in the solid ^{119}Sn-NMR spectrum at Li/Sn = 3. These facts strongly suggest that the insertion reaction is not simple as expressed by equation (8). Thus, equation (8) should be modified to be (as Li$_2$O plays essentially no role at Li/Sn > 2, it is omitted in equations hereafter)

$$Sn(\beta) + 1(Li^+ + e^-) \rightarrow \text{mixture of LiSn}_2, \text{LiSn, Li}_7\text{Sn}_2 + \text{Sn}(\beta). \tag{8'}$$
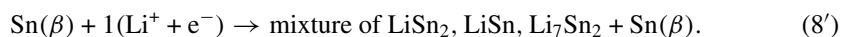
When the lithium–tin ratio exceeds four, the intensity of the component L_i increases and the total line shape becomes sharper. The atomic percentiles of L_m and L_i components are calculated from the area of the resonance line in figure 6 and the variation of atomic percentages
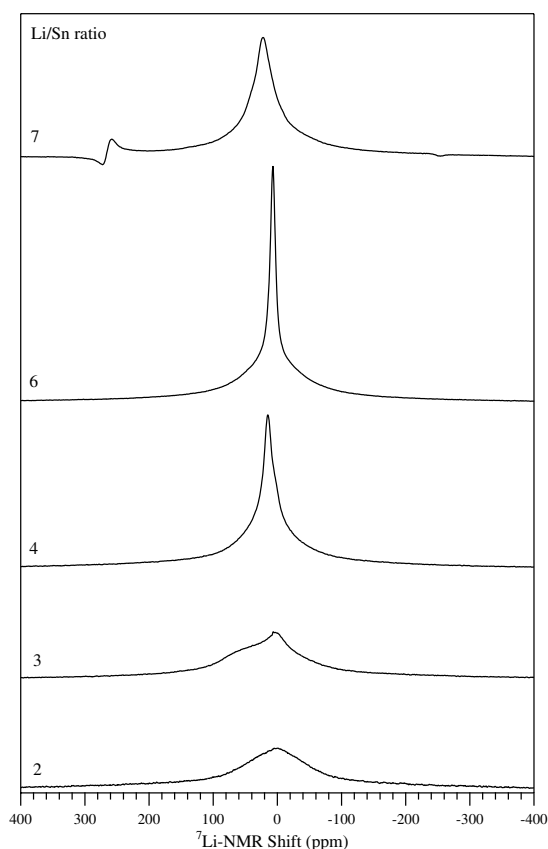
Figure 5. Solid ^{7}Li-NMR spectra of lithium-inserted SnO. The numbers at the left side show the lithium–tin ratios.

of L_m and L_i components against lithium–tin ratio is plotted in figure 7. From this plot, the metallic alloys (LiSn and LiSn$_2$) are minor components and the contribution is less than 10% between Li/Sn = 1 and 6. The quantity of component L_i increases as Li/Sn ratio increases; however, the sum of component L_m and L_i is less than 30% throughout the insertion reactions. This implies that there are ionic lithium–tin alloys with low mobility and lithium oxide in component L_b and G_b between Li/Sn = 3 and 6.

The dependence of ^{7}Li-NMR shift of three Lorentzian components, L_b, L_m and L_i, upon lithium–tin ratio is summarized in figure 8. The ^{7}Li-NMR shift of L_m decreases from 61 ppm (Li/Sn = 3) to 21 ppm (Li/Sn = 6) as the lithium insertion reaction proceeds. This fact indicates that the metallic character of the L_m component decreases during the reaction and the ionic Li$_5$Sn$_2$ alloy is the major contribution to the L_m component at Li/Sn = 6. The other component L_i shows its ^{7}Li-NMR shift between 0 and 15 ppm during the insertion reaction and is assigned to the ionic Li$_7$Sn$_2$ alloy or the ionic Li$_5$Sn$_2$ alloy. Thus the reaction products (L_m and L_i) at Li/Sn = 6 are the mixtures of the ionic Li$_7$Sn$_2$ alloy and the ionic Li$_5$Sn$_2$ alloy. The lithium insertion reaction from Li/Sn = 4 to 6 may be described as follows:

$$\text{Sn}(\beta) + 2\text{--}4(\text{Li}^+ + \text{e}^-) \rightarrow \text{mixture of Li}_5\text{Sn}_2 \text{ and Li}_7\text{Sn}_2. \tag{9}$$

The metallic lithium is detected at 265 ppm in the ^{7}Li-NMR spectrum at Li/Sn = 7 (see figure 5). Phase distortion of the metallic lithium peak occurs and this may be caused by the

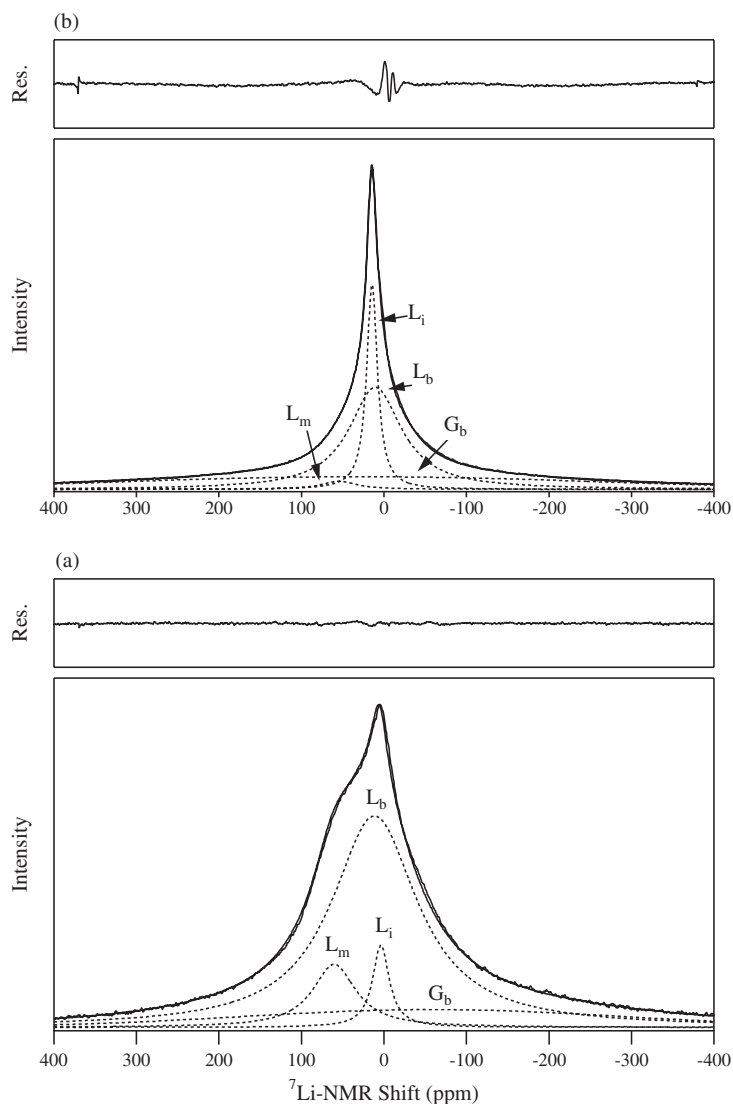**Figure 6.** Curve fitting results for solid ^{7}Li-NMR spectra of lithium-inserted SnO, (*a*) for Li/Sn = 3 and (*b*) for Li/Sn = 4. The upper half of each figure shows the residual. The assignments of L_b, G_b, L_m and L_i components are described in the text.

skin depth effect at the detection coil. This result shows that the tin (II) oxide compound cannot accept more than six-equivalent lithium.

To characterize the main reaction products in detail, the measurements of the spin–lattice relaxation time T_1 were performed for Li/Sn = 2, 3 and 6 samples. The temperature dependence of T_1 relaxation rate (T_1^{-1}) is plotted between 193 K and 393 K in figure 9. As is shown in figure 9, the plot of these samples acceptably gives a straight line. In contrast, the plot of $\ln[(T^2 T_1)^{-1}]$ versus $1/T$ does not give a straight line. Thus the spin–lattice relaxation is governed mainly by the dipole–dipole mechanism and the contribution of the conduction electrons is small for these samples. The reaction products expressed by equations (7), (8$'$)
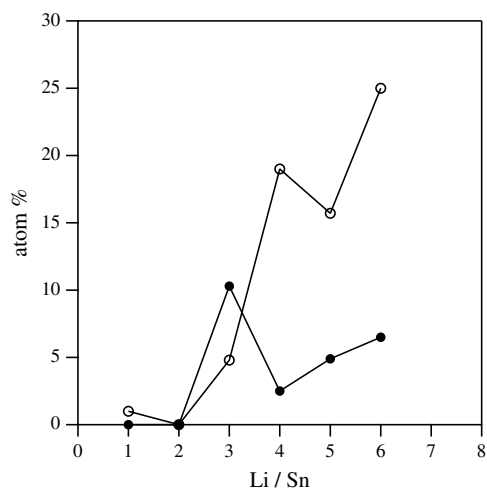
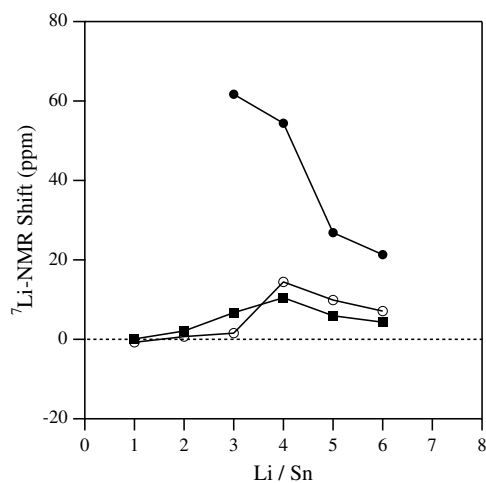**Figure 7.** At.% of L_m (●) and L_i (○) components in lithium-inserted SnO.

Figure 8. Solid ^{7}Li-NMR shift change of lithium-inserted SnO for L_m (●), L_i (○) and L_b (■) components.
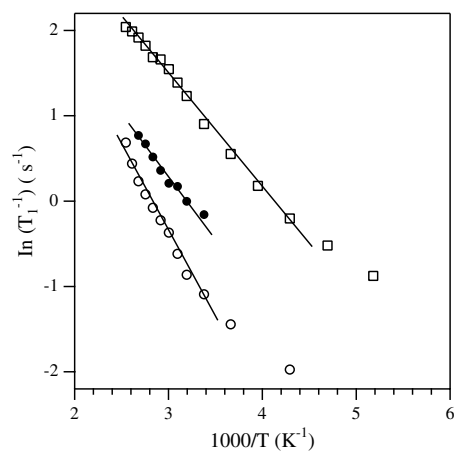

Figure 9. Temperature dependence of T_1 relaxation rate for lithium-inserted SnO: Li/Sn = 2 (○), Li/Sn = 3 (●) and Li/Sn = 6 (□).
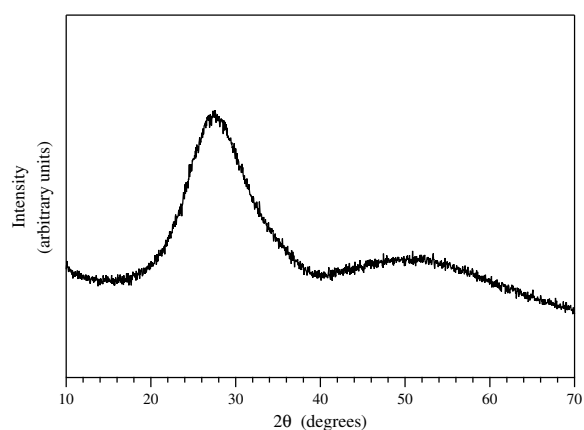

Figure 10. XRD pattern of lithium-inserted TBCO. The current density of the charging process is set to 42.4 A kg^{-1}.
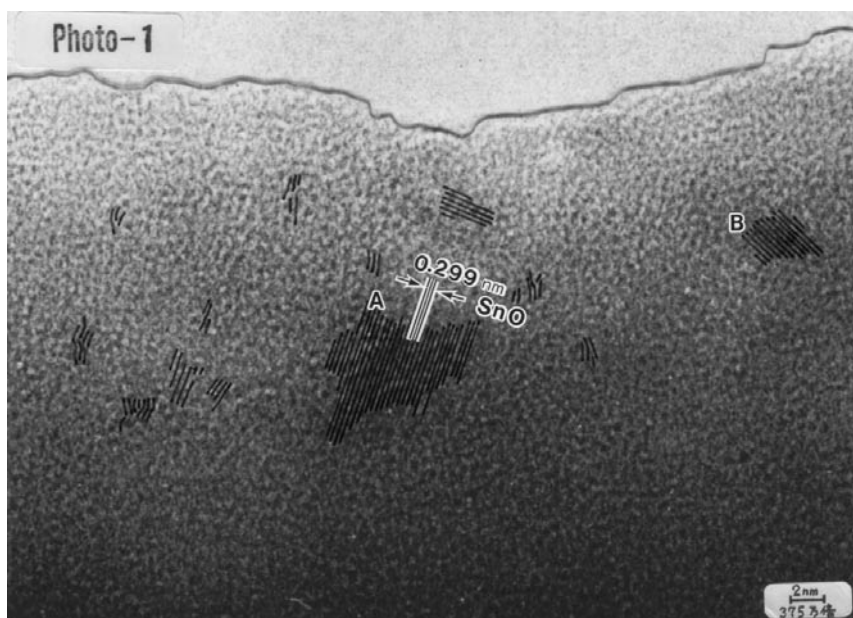
Figure 11. High resolution transmission electron micrograph of TBCO.

and (9) are supported by the behaviour of T_1 relaxation rate, too. The activation energies of the lithium ionic motion in lithium-inserted tin (II) oxides with Li/Sn = 2, 3 and 6 ratios are determined to be 16.8, 12.2 and 10.8 kJ mol^{-1}, respectively. As the lithium insertion proceeds, the activation energy becomes smaller and this behaviour corresponds to the narrowing of the line width of solid ^{7}Li-NMR spectra. The concept of 'ionic alloy' or 'zero alloy' proposed by van der Marel is confirmed for tin (II) oxide compounds even in the solid state.

3.3. Lithium-inserted tin oxide composites (TBCO)

The powder x-ray diffraction pattern of tin (II) composite oxide ($Sn_{0.8}Si_{0.5}B_{0.3}P_{0.2}Al_{0.2}O_x$, alias TBCO) is shown in figure 10. The XRD pattern is very broad and is so-called amorphous. The simple calculation using the Scherrer equation gives the average radius size of 5×10^{-10} m for crystalline region of TBCO. The high-resolution transmission electron micrograph of TBCO is shown in figure 11. The TBCO sample is mainly constituted of randomly distributed, very short-range (order of 10^{-9} m) regions and the TBCO sample is truly amorphous. Regions with relatively large crystalline of $5{-}10 \times 10^{-9}$ m in size are also found, but the number of these regions is small. The lattice spacing of A and B part in figure 11 is measured to be 3.0×10^{-10} m and this corresponds to the lattice spacing of the SnO(101) plane (2.99×10^{-10} m).

The lithium insertion reactions into TBCO are analysed by solid ^{7}Li-NMR. The solid ^{7}Li-NMR spectra of TBCO with lithium tin ratio up to 10 are summarized in figure 12. In contrast to the results obtained in the tin (II) oxide, the emergence of lithium metal is not observed until Li/Sn = 10. At Li/Sn = 9, the shoulder peak at 46 ppm is first observed and this is assigned to the lithium inserted into the graphite [17]. In the case of the TBCO compound, TBCO seems to be able to accept up to eight-equivalent lithium in the charging process. It is estimated that the silicon component in TBCO, which belongs to the same group (IV) as tin, can form lithium–silicon alloys in TBCO. The structures and physical properties
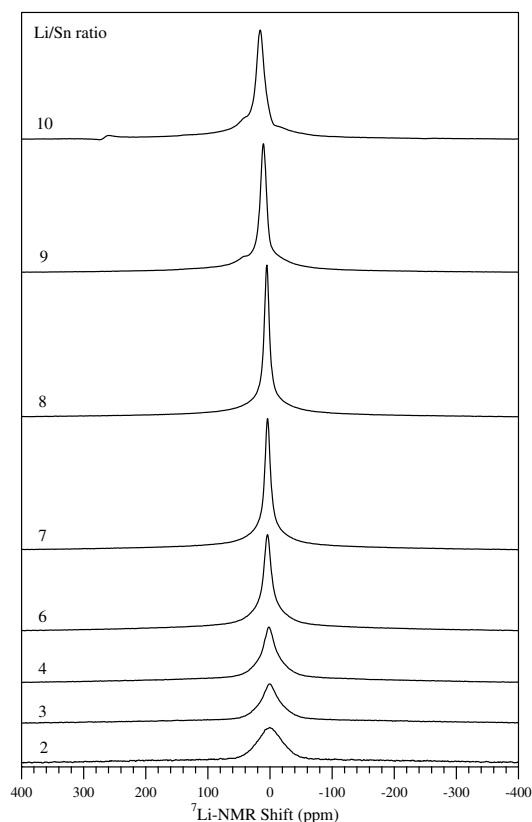
Figure 12. Solid ^{7}Li-NMR spectra of lithium-inserted TBCO. The numbers at the left side show the lithium–tin ratios.

of lithium–silicon alloys are also reported in [9] and [18].

Between the lithium–tin ratio of 2 and 8, the ^{7}Li-NMR spectra are divided into two components, the sharp Lorentzian component (alias L_x) and the broad Lorentzian component (alias L_y). The component L_x as well as the component L_y both show their ^{7}Li-NMR shift at around 0 ppm and the peak shape becomes sharp as Li/Sn ratio increases. This means that the components L_x and L_y are both highly ionic between lithium–tin ratios of 2 and 8 and are assigned to Li_7Sn_2 (and Li_7Si_2) alloy(s). The difference of these two components is the line width, which reflects the mobility in TBCO, so that the mobility of the ionic alloy (Li_7Sn_2) increases as the lithium–tin ratio increases. The component L_m, which is observed at 60 ppm and assigned to $LiSn_2$ and $LiSn$ alloys in tin (II) oxide, is not found during the charging process in TBCO.

Figure 13 shows the atomic percentages of components L_x and L_y. The residual part is attributed to the Gaussian component G_b. While the amount of component L_y keeps constant, the quantity of component L_x increases linearly at Li/Sn > 2. This implies that the mobility of lithium inserted into TBCO is relatively low at first, then the lithium with relatively high mobility appears. It is difficult to evaluate the contributions of Li_7Sn_2 alloy and Li_7Si_2 alloy to components L_x and L_y. The lithium insertion reaction from Li/Sn = 2 to 8 may be described as follows:

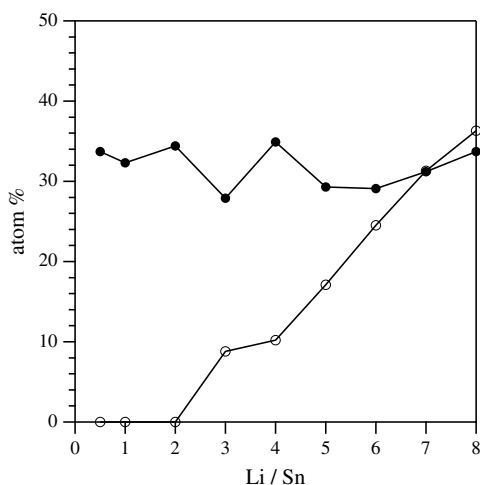$$Sn(\beta) + 2\text{–}4(Li^+ + e^-) \rightarrow Li_7Sn_2 \tag{10}$$

Figure 13. Change of at.% of L_x (○) and L_y (●) components during the insertion reaction in TBCO.

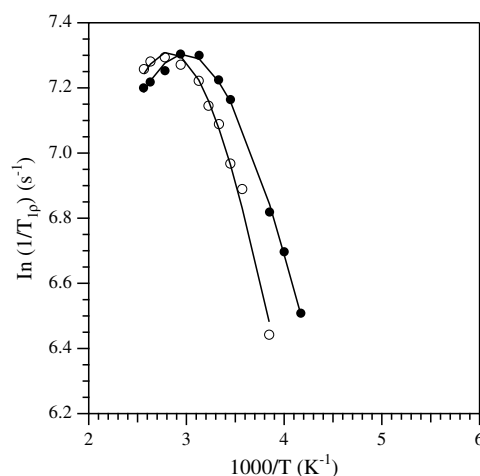**Figure 14.** Temperature dependence of $T_{1\rho}$ relaxation rate of lithium-inserted TBCO at 83 kHz magnetic field: Li/Sn = 5 (○) and 8 (●).

and

$$Si + 2\text{–}4(Li^+ + e^-) \rightarrow Li_7Si_2 \tag{11}$$

where the reaction of forming Li_2O at Li/Sn = 2 is omitted as in case of tin (II) oxide.

Since the change of ^{7}Li-NMR shift for L_x and L_y components is smaller than ± 10 ppm from Li/Sn = 0.5 to Li/Sn = 8, it is estimated that the amorphous structure of TBCO allows the formation of more ionic and stable lithium–tin alloy throughout the insertion reaction. This is in contrast to the reactions in the more rigid tin (II) oxide material.

The T_1 relaxation rate from 173 K to 393 K for lithium–tin ratio of 5 and 8 is measured at 116 MHz resonance frequency (MSL300 spectrometer); however, it is impossible to detect the T_1 minimum point. The resonance frequency is lowered to 15.5 MHz by using a CXP40 spectrometer; the T_1 minimum point is still not observed. Then, the rotating frame T_1 relaxation time ($T_{1\rho}$) is measured at 83 kHz rotating magnetic field. Finally the T_1 minimum point is found at around 350 K and the result is plotted in figure 14. The solid curves in figure 14 correspond to the theoretical ones by using equations (3) and (4). For the TBCO with Li/Sn = 5 (8) sample, the activation energy is 12.9 (10.9) kJ mol^{-1} and the inverse of attempt frequency (τ_c) is 9.2(15.2) $\times$ 10^{-8} s, respectively. The activation energies of the TBCOs with lithium is almost the same as those of the lithium-inserted tin (II) oxides. Assuming that the average jump length of the lithium ion is 4 Å, the diffusion constant in TBCO is estimated to be of the order of 10^{-15} m^2 s^{-1} at 300 K. These results clearly show that the dipole–dipole relaxation mechanism is the main path for lithium in TBCO. The ionic character of lithium–tin (and lithium–silicon) alloy(s) formed in TBCO is confirmed again by the $T_{1\rho}$ and T_1 relaxation measurements.

4. Conclusions

In the present study, the reactions of lithium insertion into tin (II) oxide and TBCO are studied in detail by the solid ^{7}Li NMR Knight shift, the T_1 ($T_{1\rho}$) relaxation rate, *in situ* XRD and TEM observations. It is shown that the formations of Li_2O and metallic tin are commonly

observed both for tin (II) oxide and TBCO up to Li/Sn = 2. At Li/Sn = 3 for tin (II) oxide, the $LiSn_2$ and LiSn alloys with usual metallic character are formed, then the ionic Li_5Sn_2 and Li_7Sn_2 alloys are formed between Li/Sn = 4 and 6. The insertion reactions are complicated. For TBCO material, the formation of Li_7Sn_2 (and Li_7Si_2) alloy(s) takes precedence over the stoichiometric lithium–tin alloys between Li/Sn = 2 and 8. The highly ionic character of the Li_7Sn_2 alloy is fully confirmed by solid ^7Li NMR shift and T_1 relaxation rate analyses.

Acknowledgments

References

[1] Idota Y, Kubota T, Matsufuji A, Maekawa Y and Miyasaka T 1997 *Science* **276** 1395
[2] Idota Y, Mineo Y, Matsufuji A and Miyasaka T 1997 *Denki Kagaku* **65** 717
[3] Courtney I A and Dahn J R 1997 *J. Electrochem. Soc.* **144** 2045
[4] Courtney I A and Dahn J R 1997 *J. Electrochem. Soc.* **144** 2943
[5] Courtney I A, Dunlap R A and Dahn J R 1999 *Electrochim. Acta* **45** 51
[6] van der Marel C, Geertsma W and van der Lugt W 1980 *J. Phys. F: Met. Phys.* **10** 2305
[7] van der Marel C, van Oosten A B, Geertsma W and van der Lugt W 1982 *J. Phys. F: Met. Phys.* **12** 2349
[8] Alblas B P, van der Lugt W, Dijkstra J and van Dijk C 1984 *J. Phys F: Met. Phys.* **14** 1995
[9] van der Lugt W 1996 *J. Phys.: Condens. Matter* **8** 6115
[10] Müller W and Schäfer H 1973 *Z. Naturf.* b **28** 246
[11] Hansen D A and Chang L J 1969 *Acta Crystallogr.* B **25** 2392
[12] Frank U, Müller W and Schäfer H 1975 *Z. Naturf.* b **30** 1
[13] Frank U, Müller W and Schäfer H 1975 *Z. Naturf.* b **30** 6
[14] Korringa J 1950 *Physica* **16** 601
[15] Dupree R, Kirby D J and Warren W W Jr 1985 *Phys. Rev.* B **31** 5597
[16] Farrar T C and Becker E D 1971 *Pulse and Fourier Transform NMR—Introduction to Theory and Methods* (NewYork: Academic) p 46
[17] Conard J, Nalimova V A and Guerard D 1994 *Mol. Cryst. Liq. Cryst.* **245** 245
[18] Meijer J A, van der Marel C, Kuiper P and van der Lugt W 1989 *J. Phys.: Condens. Matter* **1** 5283